ACS APPLIED MATERIALS & INTERFACES

Research Article

www.acsami.org

Aligned Bioinspired Cellulose Nanocrystal-Based Nanocomposites with Synergetic Mechanical Properties and Improved Hygromechanical Performance

Baochun Wang,[†] Jose Guillermo Torres-Rendon,[†] Jinchao Yu,[‡] Yumei Zhang,[‡] and Andreas Walther*,[†]

[†]DWI—Leibniz-Institute for Interactive Materials, RWTH Aachen University, Forckenbeckstr. 50, 52056 Aachen, Germany

[‡]State Key Laboratory for Modification of Chemical Fibers and Polymer Materials, Donghua University, 201620 Shanghai, China

Supporting Information

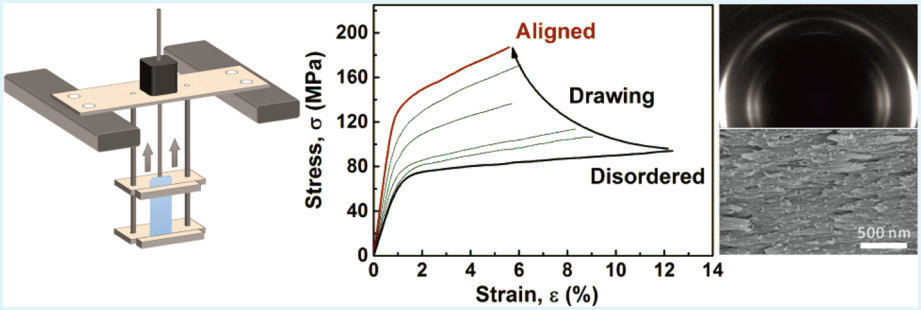

ABSTRACT: Natural high-performance materials inspire the pursuit of ordered hard/soft nanocomposite structures at high fractions of reinforcements and with balanced supramolecular interactions. Such biomimetic design principles remain difficult to realize for bulk nanocomposites. Herein, we establish an effective drawing procedure that induces a high orientation of crystalline cellulose nanocrystals (CNCs) in a matrix of carboxymethylcellulose (CMC) at high level of reinforcements (50 vol %). We show such alignment in rather thick bulk films and report synergetic improvement with a simultaneous increase of stiffness, strength, and work-to-fracture as a function of the degree of alignment. Scanning electron microscopy and two-dimensional X-ray diffraction quantify the alignment of the cylindrical nanoparticles and link it to the extent of drawing and improvements in mechanical properties. We further show that the decline in mechanical properties of such waterborne all biobased nanocomposites at high relative humidity can be balanced using supramolecular modulation of the ionic interactions by exchanging the monovalent Na^+ counterion, present in CMC and CNC with di- or trivalent Cu^{2+} and Fe^{3+}. This contribution demonstrates the importance of aligning one-dimensional reinforcements to achieve synergetic improvement in mechanical properties in sustainable bioinspired nanocomposites and suggests pathways to prepare water-stable materials based on a waterborne processing route.

KEYWORDS: *nanocellulose, bioinspired materials, toughness, humidity, wet-drawing*

INTRODUCTION

The quest for sustainable materials engineering requires developing materials with competitive mechanical and functional performance based on renewable resources and using energy-efficient and benign preparation pathways. Cellulose-based materials are one of the prime candidates because cellulose is the most abundant biomaterial on our planet, rapidly growing, biocompatible, biodegradable, and of rather low-cost. Polymeric cellulose has been the basis for products in our daily lives, ranging from fibers to textiles, cellophane, and as texturizer in colloidal products and food. Recently, nanocellulose materials, which can be divided into cellulose nanocrystals (CNC) and cellulose nanofibrils (NFC), have moved into the focus of materials research due to their extraordinary mechanical properties.[1−13] CNCs are rod-like cylindrical particles that are easily prepared by acidic hydrolysis from a range of cellulose-containing feedstock. Most common sources are cotton,[14,15] plant fibers,[16−24] treated pulps,[25−27] microcrystalline cellulose,[28−30] bacterial cellulose,[31−33] and tunicates.[34−36] They have high aspect ratios (3−20 nm in width and 50−500 nm in length for most plant-based CNCs) and a high degree of crystallinity. Their stiffness is near 143 GPa, and their tensile strength has been estimated to be in the order of 10 GPa.[37,38] Most importantly, and in contrast to what can be achieved by recrystallization, natural selection has allowed the growth of these cellulose nanocrystals with nanoscale dimensions that are optimized for high fracture toughness, among fulfilling other functional plant requirements.[39]

Received: November 5, 2014
Accepted: February 3, 2015
Published: February 3, 2015

DOI: 10.1021/am507726t
ACS Appl. Mater. Interfaces 2015, 7, 4595−4607

Cellulose microfibrils, a primary source for cellulose nanomaterials, are the reinforcing components in biological tissues. In wood, the reinforcing cellulose microfibrils are embedded in the walls of the wood cells and aligned within an energy-dissipating soft matrix containing hemicellulose and lignin.[40] This nanocomposite material is optimized for high stiffness, strength, and high fracture toughness, while also certainly addressing other biological constraints. The soft layer between the microfibrils allows for deformation, despite the high level of reinforcements. Helical winding (cellulose microfibrillar angle) of the structures enhances mechanical strength (in particular for compression) and allows for hydromechanical actuation.[41] Such sophisticated biological architectures teach us design principles for bioinspired nanocomposite materials.[42] In bioinspired nanocomposite materials, ordered structures of stiff anisometric reinforcing particles are pursued within a tailored soft phase, at best containing molecularly designed energy dissipation mechanisms. Owing to the natural design principles, such ordered structures need to be pursued at high fractions of reinforcement, that is, at biomimetic compositions.

Inorganic nanoparticles have traditionally been used as reinforcements in polymeric materials to create nanocomposite materials.[43] Such nanocomposites have been optimized to comply with traditional processing techniques and typically contain fairly less than 10 wt % of reinforcing nanoparticles (e.g., nanoclay). Said nanocomposites typically exhibit an enhancement of stiffness and strength, but mostly sacrifice strain-to-failure. Synergistic increase of stiffness, strength and toughness remains difficult to achieve in such traditional approaches. In the framework of nanoclay-based nanocomposites, great progress could recently be demonstrated by applying biomimetic design principles inspired by the nacreous layer of sea shells (high fraction of reinforcements and high degree of order and alignment) to polymer/clay nanocomposite. Such nacre-mimetic nanocomposites have generated mechanical stiffness and strength being typically an order of magnitude higher than what could be achieved in traditional nanoclay/polymer nanocomposite materials.[44−54] This inspires to apply similar design principles to nanocellulose building blocks.

The mechanical properties of nanocellulose have already been translated into mechanically interesting materials. NFC has been used to create pure[55−59] and nanocomposite[60−69] nanopapers, as well as fibers[70−72] and foams[73−75] with attractive mechanical properties. Similarly, there exists significant literature on using CNCs in the framework of traditional nanocomposites with low fractions of reinforcement and often disordered structures.[4] CNCs are very difficult to align in a unidirectional fashion and high magnetic or electric fields[76−82] were suggested. Interestingly enough, unidirectional alignment at high fractions of wood-based CNCs requires rotating magnetic fields to unwind the helical structure of the otherwise occurring cholesteric mesophase.[78] Ultrathin oriented films can be prepared by shear alignment and convective forces using CNC suspensions,[83−86] also in combination with electric fields,[87] while specialized cylindrical rotational shearing units with in situ drying may allow shear-orientation in thicker films.[88] Other approaches have shown that the helical cholesteric structure formed by self-assembly of CNCs can be stabilized by cross-linking with resins during/after film formation from molecular precursors[89−95] or via cocasting with nonionic polymers in organic solvent.[96] Toward unidirectionally aligned larger-scale CNC-based materials, fiber spinning of cellulose diacetate,[97] alginate,[98,99] poly(vinyl alcohol)[100,101] with CNCs allowed to make ordered fibers with CNC loading up to 10−50 wt %. In general, preferential alignment and order is not only important for mechanical reinforcement but also plays a decisive role in imparting anisotropic optical and thermal properties that could be tuned according to a targeted application.

One of the major bottlenecks of nanocellulose particles is their highly hydrophilic nature. On the one hand this leads to difficulties in combining them with hydrophobic matrix polymers, and on the other hand this leads to nanocomposites that are inherently susceptible to humidity. For instance, we recently described in detail how humidity influences the mechanical performance of cellulose nanopapers across the full elastic and plastic regime.[102] First approaches to stabilize the mechanical properties of waterborne cellulose-based materials with defined chemical interactions have, for instance, been reported by combination with chemically modified polymers[51] or ionic interaction.[45] Moreover, if ordered materials are targeted, the highly polar and charged nature of the nanocellulose building blocks mostly requires to use water for colloid-based solution processing and assembly of nanocellulose in combination with water-soluble polymers. To this end, the combination with polysaccharides becomes important as this allows fully waterborne routes with all-biobased building blocks. The focus of this contribution will be on CNCs. Such CNCs were previously combined with water-soluble polysaccharides to prepare classical disordered nanocomposites at low fractions of reinforcements, also often only offering little insights into structure and detailed understanding and modulation of mechanical properties.[4,12,103]

Herein, we will combine CNCs with sodium carboxymethyl cellulose (CMC) to prepare solution-cast all biobased nanocomposite films up to very high levels of reinforcements. We will demonstrate that mechanical drawing of films under plasticized conditions containing 50 wt % of reinforcing materials can be used to achieve nematic-type, unidirectional alignment of the reinforcing CNCs in quasi bulk conditions. The resultant materials show synergetic improvement with a simultaneous increase of stiffness, strength and toughness. We also address better mechanical performance at high relative humidity by exploiting the carboxylic and sulfonic acid functionalities on the building blocks using supramolecular ionic cross-linking based on infiltration of multivalent counterions. The resulting materials are first examples of ordered (near bulk) thick films combining highly aligned, bioinspired, mesoscale structures with synergetic improvement and stability at high relative humidity.

EXPERIMENTAL SECTION

Materials. Whatman filter paper (grade 1, Aldrich). Sodium carboxymethyl cellulose (CMC, M_w = 90 kg·mol^{-1}, degree of substitution (DS) = 0.9, Aldrich). Milli-Q water was used for all experiments.

Preparation of Cellulose Nanocrystals (CNCs). CNCs were isolated from Whatman filter paper via acid hydrolysis with 64% H_2SO_4 at 70 °C for 30 min. The reaction was quenched by putting the reaction flask into an ice bath. The suspension was washed three times by centrifugation at 8000 rpm for 30 min. The resultant slurry was dialyzed against deionized water for several days to remove excess acid, low molecular weight carbohydrates, and other water-soluble impurities. The final pH was constant around 4−5. The CNC suspension was then ultrasonicated for 2 h.

DOI: 10.1021/am507726t
ACS Appl. Mater. Interfaces 2015, 7, 4595−4607

Scheme 1. Preparation, Alignment and Supramolecular Modulation of Properties in CNC/CMC Nanocomposites[a]

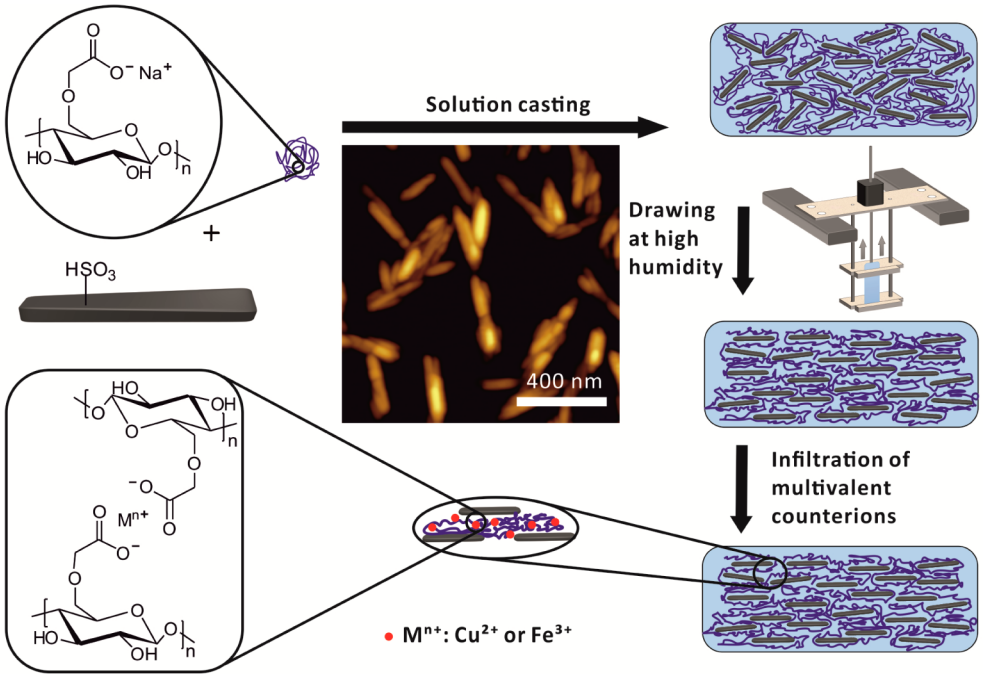

[a]The center AFM image depicts the used rod-like CNCs (see Figure S1, Supporting Information for statistical evaluation).

Preparation of CNC/CMC Nanocomposite Films. The CNCs were diluted to a 0.5 wt % dispersion overnight and subsequently slowly added to a strongly stirred 0.25 wt % solution of CMC until the desired weight ratio was obtained. The mixed suspension was then subjected to ultrasonic bath for 20 min to reduce any aggregation that may have occurred during the mixing process. This dispersion was then poured into a plastic dish and air-dried for 3−4 days.

Ionic Supramolecular Cross-Linking. Infiltration of the nanocomposite film was done by placing the films (ca. 200 mg) into a 0.1 M copper sulfate or 0.05 M iron(III) sulfate solution (100 mL) for 3 days. Excess ions/salt were removed by washing in deionized water, leaving strongly colored films after drying.

Drawing at High Relative Humidity (RH). We built a wet/humidity-drawing device based on aluminum profiles and a computer-controlled linear actuator (Haydon Kerk stepper motor 21000 series size 8) able to perform strain-controlled drawing. CMC/CNC films with gauge lengths of 10 cm (width 1 cm, thickness 40−50 μm) were clamped in the device and put into a humidity chamber of 99% RH. After relaxation, the films were subjected to a periodic drawing routine. The draw velocity was set to 2 mm/min, and the drawing process was interrupted for 10 min every 10 mm of drawing to release excess stress. The specimens were left inside the drawing device for an additional 2 h, dried within the drawing clamps, and thereafter removed. During stretching, the major deformation occurs laterally, meaning the sample loses width rather than thickness.

Mechanical Properties. Tensile tests were carried out on a DEBEN minitester equipped with a 20 N load cell at room temperature. The samples were conditioned at the specified relative humidities (RH) for at least 24 h. The specimen sizes used were 1.5 cm × 1.25 mm × 40−50 μm using a gap width of 1 cm. At least seven specimens were tested for each condition. A nominal strain rate of 0.5 mm·min^{-1} was used (1 mm·min^{-1} was also used). The slope of the linear region of the stress/strain curves was used to determine the Young's modulus (E).

Field-Emission Scanning Electron Microscopy (FE-SEM). Film surfaces and fracture surfaces were observed by a Hitachi S4800 FE-SEM. The samples were sputter coated with a thin gold/palladium layer.

Wide Angle X-ray Diffraction (WAXD). WAXD experiments were carried out at the beamline BL14B1 at the Shanghai Synchrotron Radiation Facility (SDRF) with a wavelength of 0.12398 nm. The sample cell was placed in a sample holder perpendicular to the X-ray beam. The distance between the detector (Mar 345) and the sample was 332.24 mm. LaB_6 was used for calibration. A typical acquisition time was 60 s. The patterns were corrected for air scattering and background. The azimuthal intensity distribution profiles along the arc that refers to the (200) reflections of the cellulose Iβ crystals[98] were used to quantify the orientation of the CNC rods along the films. This peak is determined to be within 2θ = 22.0−22.4°. Intensity distribution profiles in the azimuthal angle (ϕ) were used to calculate the orientation index (π) and the order parameter (S) according to the equations:

$$\pi = \frac{180^\circ - \text{fwhm}}{180^\circ}$$

$$S = \frac{3\cos^2\phi_{c,z} - 1}{2}$$

$$\cos^2\phi_{c,z} = 1 - 2\cos^2\phi_{200,z}$$

$$\cos^2\phi_{200,z} = \frac{\sum_0^\pi I(\phi)\sin\phi\cos^2\phi}{\sum_0^\pi I(\phi)\sin\phi}$$

where fwhm is the full width of the half-maximum of the azimuthal profiles from the selected equatorial reflection, and I(ϕ) is the intensity distribution along the Debye−Scherrer ring.[84,88,97,98]

Atomic Force Microscopy (AFM). Atomic force micrographs of CNCs were taken using a NanoScope V (Digital Instruments Veeco Instruments, Santa Barbara, CA) AFM operating in tapping mode. The sample was obtained by dip-coating from a diluted suspension in water (0.002 wt %) onto freshly cleaved mica.

RESULTS AND DISCUSSION

Our general strategy is sketched in Scheme 1. It starts with the nanocomposite preparation based on a waterborne film casting route of CNC in combination with NaCMC. This is followed by mechanical drawing under plasticized conditions at high

DOI: 10.1021/am507726t
ACS Appl. Mater. Interfaces 2015, 7, 4595−4607

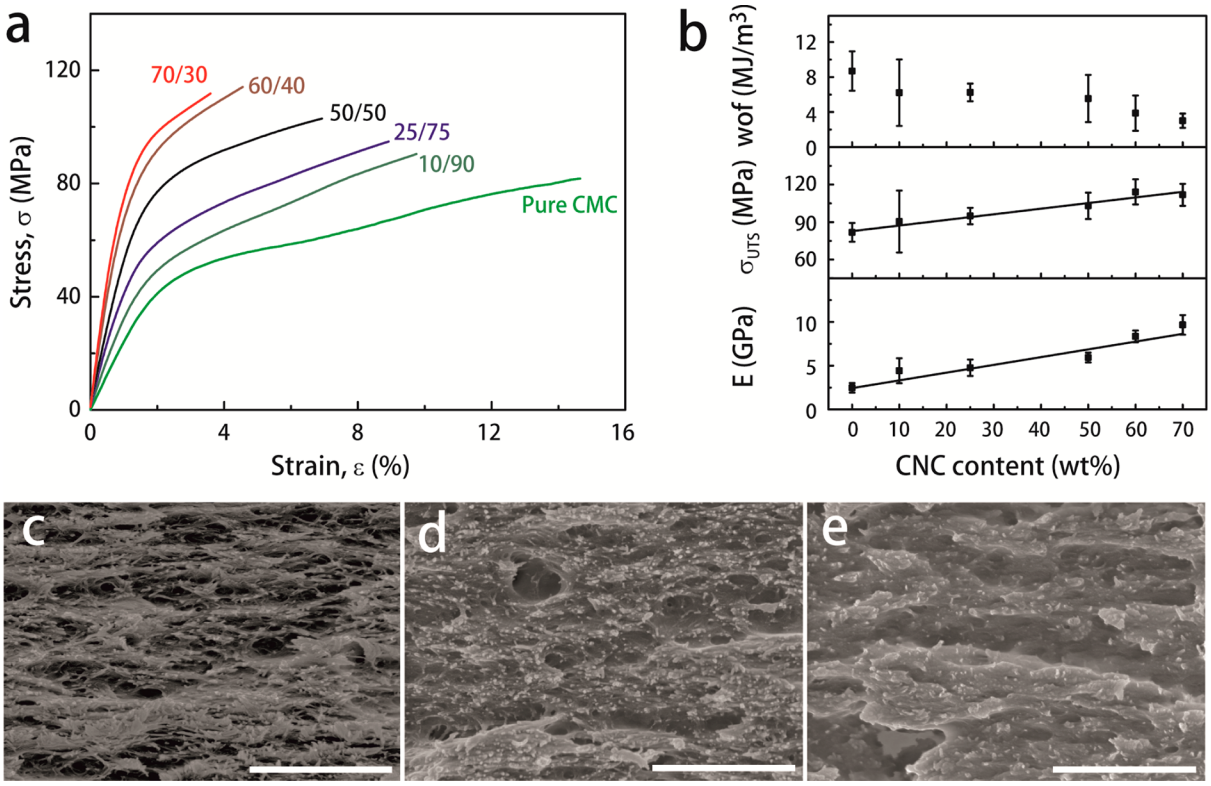

Figure 1. Tensile mechanical properties and mesostructure of CNC/CMC nanocomposites as a function of composition. (a) Stress/strain curves at various compositions as indicated within the figure and at 60% RH. (b) Overview of Young's modulus, E, tensile strength, σ_{UTS}, and work-of-fracture, wof, as a function of CNC content. The lines are a guide to the eye. SEM images of fractured cross sections of CNC/CMC = (c) 90/10, (d) 50/50, and (e) 10/90 w/w (scale bars are 1 μm).

relative humidity to allow for an alignment of the nanoscale reinforcements. The aligned films with maximized properties are subsequently subjected to a simple infiltration of multivalent counterions to modulate the supramolecular interactions and target mechanical stability at high relative humidity.

The CNCs were isolated via the classical acidic hydrolysis route[104] from cotton filter paper and were characterized by AFM to give an average length of 165 ± 51 nm, and a height of 9 ± 2 nm (Supporting Information, Figure S1). Such pristine CNC dispersions are known to form cholesteric liquid crystals during film casting due to an interplay of the negatively charged groups and the twisted ribbon shape of the rod-like colloids.[105] The corresponding CNC films are inherently brittle due to the lack of interstitial polymers able to dissipate fracture energy. We choose anionic CMC as a suitable polymer for providing a soft phase between the CNCs. CMC is an attractive polysaccharide due to its good inherent mechanical properties and moreover due to the presence of carboxylic acid groups which can be used to manipulate interactions within the bulk phase and with the sulfonate-group containing CNCs by changing the valency of the counterions.[44,45]

The ratios for the CNC/CMC nanocomposites were selected in a wide range (70/30, 60/40, 50/50, 40/60, 25/75, 10/90 w/w) to monitor the full behavior of the system and with a particular emphasis on high fractions of reinforcements. Due to similar densities of CNC and CMC (Na^+ counterion; ρ_{CNC} = 1.56 g·cm^{-3}, and ρ_{CMC} = 1.60 g·cm^{-3}), the volume ratios are closely identical with the weight ratios. Below, we will rationalize how lateral interparticle distance between CNCs scales with polymer content in a hexagonally closed packing scenario. The nanocomposites were simply prepared by slowly dripping a CNC dispersion (0.5 wt %) to a CMC solution (0.25 wt %) until the desired composition is reached and subsequent evaporation. The addition of the nanoparticle dispersion to the polymer solution minimizes potential aggregation of nanoparticles. Macroscopically, all films are fully transparent and are thus different to pure CNC films, which show iridescence due to the Bragg reflections of the cholesteric nematic phase. Indeed, and also to our surprise, even films with 95 wt % of CNCs no longer show any cholesteric phase, possibly due to an interference of the anionic CMC with the self-assembly process of the anionic CNCs during evaporation. The differences can be traced by polarized optical microscopy (POM) and scanning electron microscopy. POM micrographs are black and do not show fingerprint patterns (characteristic of the cholesteric phase, not shown here), and SEM imaging of various nanocomposites displays the disordered structures (Figure 1c–e).

Next, let us turn to the mechanical behavior in tension and at 60% relative humidity (60% RH). Pure CMC displays ductile behavior with an attractive stiffness (Young's modulus) of E = 2.5 GPa, tensile strength σ_{UTS} = 83 MPa, and strain-at-break ε_{max} = 15%. Starting from pure CMC, it is obvious that continuous addition of CNC leads to a stiffening of the material up to a weight ratio of ca. 50 wt %, while the improvements begin to level of at 70 wt % CNC (Figure 1a). This behavior originates from an efficient stress transfer from the CMC matrix to the CNC reinforcements via multivalent hydrogen bonds. At 70 wt % the reinforcement efficiency declines indicating some inefficient activation of the large CNC surface area and potential CNC/CNC contacts. Tensile strength scales similarly and the best materials show a near doubling of the original

DOI: 10.1021/am507726t
ACS Appl. Mater. Interfaces 2015, 7, 4595–4607

Table 1. Mechanical Properties of CNC/CMC Nanocomposites Films as a Function of CNC Content[a]

CNC content (wt %)	Young's modulus, E (GPa)	tensile strength, σ_{UTS} (MPa)	yield stress, σ_y (MPa)	strain-at-break, ε (%)	work-of-fracture, wof (MJ·m^{-3})
0	2.5 ± 0.5	82 ± 7.5	43	15 ± 3	9 ± 2
10	4.5 ± 1.5	90 ± 25	41	10 ± 4	6 ± 3
25	5.0 ± 0.5	95 ± 6.5	51	9.0 ± 2	6 ± 1
50	6.5 ± 0.5	103 ± 10	67	7.0 ± 2	5 ± 2
60	8.0 ± 1.0	114 ± 10	68	4.5 ± 2	4 ± 2
70	10 ± 1.0	111 ± 9	72	3.5 ± 0.5	3 ± 0.5

[a]Test speed 1 mm/min.

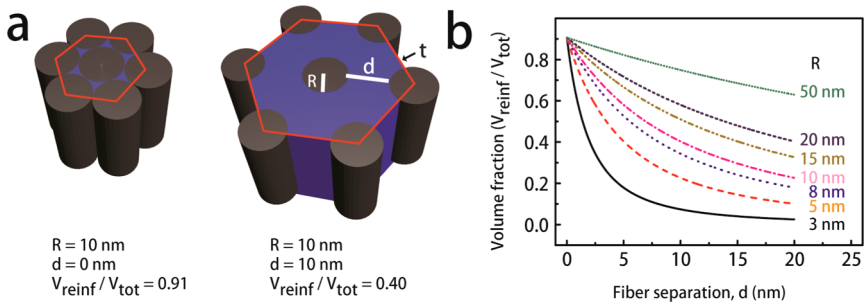

Figure 2. (a) Structural models rationalizing the geometrical constraints in unidirectionally oriented nanocomposites assuming (gray) infinitely long cylindrical reinforcements embedded in a hexagonal fashion within a (blue) polymeric matrix. (b) The corresponding calculation depicts the fiber distance as a function of the volume fraction of the reinforcements, for reinforcements of different radius as indicated within the figure.

tensile strength. After passing 50 wt % of CNC, a rapid decrease of the strain at break occurs, and the materials turn increasingly brittle due to a lack of sufficient polymer to allow for inelastic deformation, resulting in insufficient stress delocalization around crack tips and rather fast crack propagation. Additionally, potential CNC agglomerates may be a source of defects to initiate failure. The area under the curve, which can be used as an estimate for the needed work to fracture the materials (wof), stays near constant until 50 wt % CNC and then also drops to lower levels. All values are summarized in Table 1, and we find an interesting optimum performance at 50 wt % of CNC considering the need to balance the tensile strength and strain at break.

In the following, we will demonstrate how highly reinforced nanocomposite films can be aligned. From above, we identify the CNC/CMC 50/50 w/w film as the most suitable material due to optimum combination of stiffness, strength, and toughness. Before we turn to the alignment procedure, it is important to realize the structural dimensions of an ordered lattice, which can be obtained as a function of the composition and the diameter of the one-dimensional (1D) reinforcement when targeting highly ordered structures (Figure 2a). For simplicity, we have to assume an ideally ordered hexagonally packed nematic phase of infinitely long 1D reinforcements (here, CNCs elongated to infinity along their main axis). For the calculations, we consider an infinitely thin cross section of one hexagon. The area within the hexagon, A_{total}, can be calculated according to its side length, t.

$$A_{total} = \frac{3\sqrt{3}}{2}t^2 = \frac{3\sqrt{3}}{2}(d + 2R)^2$$

with $t = d + 2R$, where d is the distance between 1D reinforcements, and R is the radius of a reinforcement.

At the same time, one hexagon contains three full cross sections of the reinforcements, A_{reinf}, yielding

$$A_{reinf} = 3\cdot\pi R^2$$

This enables us to calculate their ratio (also in volumetric terms) as a function of interfibrillar distance between the reinforcements for any give radius as follows:

$$\frac{V_{reinf}}{V_{total}} = \frac{A_{reinf}}{A_{total}} = \frac{2\cdot\pi R^2}{\sqrt{3}\cdot(d + 2R)^2}$$

The plots in Figure 2b in fact demonstrate the necessity of a certain minimum fraction of polymer (>9 vol %) to prevent direct contact of the reinforcements. The influence of the diameter of the reinforcements depicted in Figure 2b further demonstrates that well-defined matrix/1D reinforcement bioinspired nanocomposites require a minimum amount of polymer to activate the entire reinforcement interface. Furthermore, the thickness of the interstitial matrix, d, between the reinforcements depends very strongly on the diameter of the reinforcements. These are important rationalizations for general attempts to surround 1D cellulose nanomaterials completely with a matrix material and the aim to change their interfibrillar interactions in biomimetic nanocomposite settings. Considering our materials, this rationalization shows that the separation distance between two CNCs in an assumed hexagonal lattice is already smaller than their diameter at the determined optimum ratio of CNC/CMC = 50/50 w/w. Considering the densities of the materials (ρ_{CNC} = 1.56 g·cm^{-3}, and ρ_{CMC} = 1.60 g·cm^{-3}) and assuming the rod-like CNCs have circular cross sections with a radius of ca. 4.5 nm (deduced from the average height of 9 nm from the statistical analysis of the AFM images), we can calculate the thickness of the interstitial matrix to be d = 3.1 nm. This value is considerably smaller than the radius of gyration of the used CMC of 90 kg·mol^{-1} and shows that the material is largely defined through interfaces and that the polymer layers exhibit nanoconfinement. Both aspects are fundamental features of biomimetic nanocomposites and add challenges to understanding the mechanical behavior.

Our approach toward alignment uses a custom-built strain-rate controlled drawing device, which can be submerged in

DOI: 10.1021/am507726t
ACS Appl. Mater. Interfaces 2015, 7, 4595−4607

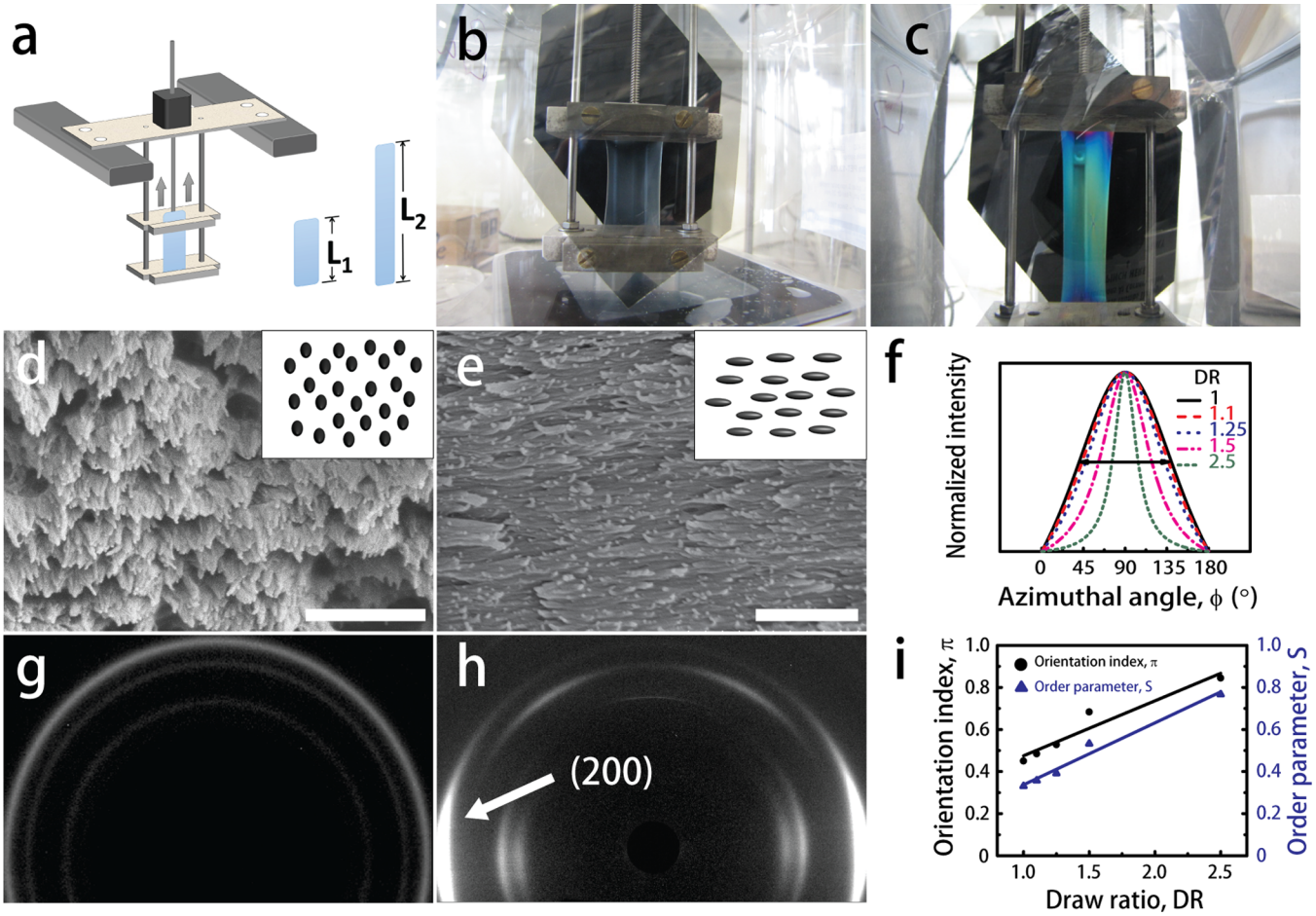

Figure 3. Alignment procedure and structural characterization for drawing of CNC/CMC films of 50/50 w/w. (a) Experimental setup and drawing ratio, DR, as defined by L_2/L_1. Photographs of (b) unstretched and (c) stretched film between crossed polarizers, demonstrating efficient alignment due to the occurrence of birefringence. SEM images of a fractured cross section of a drawn and strongly aligned film, DR = 2.5, acquired (d) perpendicular to and (e) within the drawing direction (scale bars are 500 nm). (g–i) 2D WAXD data to characterize the extent of alignment. (g and h) One half of the 2D detector images for films with (g) DR = 1 and (h) DR = 2.5. (f) Azimuthal intensity profiles with narrowing fwhm for increasing DR as indicated within the figure. (i) Orientation index, π, and order parameter, S, as a function of DR, establishing a direct link between drawing and orientation of the reinforcements.

water or conditioned at a certain level of relative humidity to allow flow and realignment even in delicate and highly reinforced nanocomposites (Figure 3a). We chose to perform this drawing in a strongly humidified environment (99% RH) to maximize the dynamics inside the materials and allow for efficient plastic deformation. The routine works as follows: Initially, a nanocomposite film with a length L_0 of about 10 cm (width, 1 cm; thickness 40–50 μm) is fixed to the clamps and allowed to equilibrate with the relative humidity inside the chamber for 1 h. Afterward, it is drawn without force into a fully straight position L_1. Then, the sample is drawn up to the desired length L_2, which defines the drawing ratio, DR = L_2/L_1. The draw velocity is set to 2 mm/min, and the drawing process is interrupted for 10 min every 10 mm of drawing to release excess stress. Overall, this gives sufficient time for efficient nanoparticle and polymer matrix rearrangement until the desired DR is reached. Once the drawing process is finished, the nanocomposites film is removed from the humidity chamber and allowed to "dry" while still being clamped inside the device. This procedure allows a drawing up to 150%, DR = 2.5. Higher drawing ratios turned out to be unreliable and typically lead to fracture.

The ongoing alignment of the film can be traced in situ by placing it between crossed polarizers. The two photographs depicted in Figure 3b,c clearly show a continuously increasing alignment inside the film due to the appearance of birefringence.

The successful alignment can be further evidenced by SEM and quantified via wide-angle X-ray diffraction (WAXD). We performed SEM imaging of the films at different DR and report images for side-on and perpendicular cross sections of a highly drawn film (DR = 2.5; Figure 3d,e). These can be compared to a nonoriented film shown above (DR = 1; Figure 1d). The most striking difference between the original and the drawn films is the near complete alignment of the CNCs clearly visible after drawing, thereby confirming that the CNCs are indeed being oriented during the drawing procedure. To quantify the alignment procedure, we performed two-dimensional (2D) WAXD at a synchrotron source and monitored how azimuthal intensity profiles of selected crystal reflections change during drawing. The setup consists of irradiating the films perpendicular to an X-ray beam. Already from the two 2D detector images of nondrawn and drawn films (DR = 1 and 2.5; Figure 3g,h), it becomes obvious that the reflections are increasingly confined into arcs, thereby suggesting an improved

DOI: 10.1021/am507726t
ACS Appl. Mater. Interfaces 2015, 7, 4595–4607

Table 2. Mechanical Properties and Degree of Alignment for CNC/CMC (50/50 w/w) Nanocomposites Films As a Function of the Draw Ratio[a]

draw ratio, DR	orientation index, π	order parameter, S	Young's modulus, E (GPa)	yield stress, σ_y (MPa)	tensile strength, σ_{UTS} (MPa)	strain at break, ε (%)	work-of-fracture, wof ($MJ \cdot m^{-3}$)
1.0	0.45	0.33	6.5 ± 0.5	61	93 ± 1	12 ± 1.5	9.8 ± 2.0
1.1	0.48	0.36	8.0 ± 1.0	67	107 ± 3	9.0 ± 1.0	7.8 ± 1.0
1.25	0.53	0.39	9.0 ± 1.0	82	114 ± 8	8.3 ± 2.3	7.7 ± 2.0
1.5	0.68	0.53	10 ± 2.0	93	137 ± 25	5.6 ± 1.1	6.0 ± 1.0
2.0	n.d.	n.d.	13 ± 4.0	117	171 ± 10	6.1 ± 3.4	8.0 ± 3.0
2.5	0.84	0.76	15 ± 2.5	151	187 ± 29	5.6 ± 2.0	8.0 ± 2.0

[a]Test speed 0.5 mm/min.

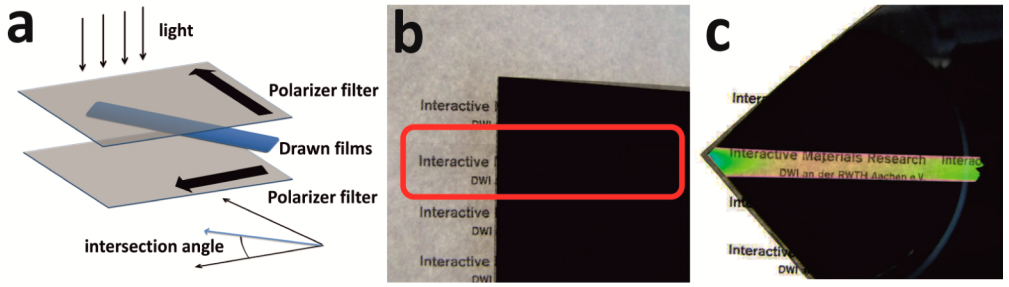

Figure 4. Birefringence and polarization features of drawn CNC/CMC = 50/50 w/w nanocomposite films (DR = 2.5) observed between crossed polarizers. (a) Drawn film between the two crossed polarizers with a certain intersection angle. (b) When the intersection angle is 0°, the overlapping part is dark, meaning that the structure is aligned parallel to one of the filters. (c) When the intersection angle is 45° in the overlapping area, the drawn film shows strong birefringence, confirming a high degree of alignment.

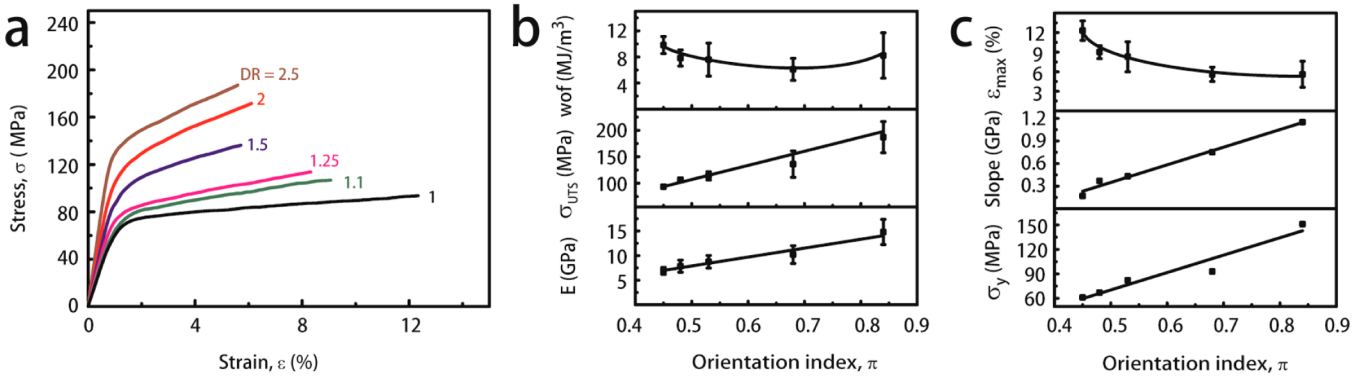

Figure 5. Mechanical properties of CNC/CMC 50/50 w/w nanocomposite films after progressive alignment. (a) Tensile tests at various DR as indicated within the plot (60% RH). (b) Overview of Young's modulus, E, tensile strength, σ_{UTS} and work-of-fracture, wof, as a function of the orientation index. (c) Overview of the yield stress, σ_y, slope in the plastic region and strain at break, ε_{max}, as a function of the orientation index. The lines are a guide to the eye.

alignment of the crystallites along the drawing axis. We traced this orientation using the crystal (200) reflection arising from the CNCs. Figure 3f displays the azimuthal intensity profiles of the mentioned reflections at different drawing ratio. The more defined profiles with more narrow fwhm at higher DR clearly confirm increasing degrees of alignment. We calculate the degree of alignment using two methods: (1) the orientation index defined as $\pi = (180° - \text{fwhm})/180°$ and (2) the order parameter defined as $S = (3/2)\langle\cos^2\phi\rangle - (1/2)$ (further details in the Experimental Section). Both dependencies are graphically depicted in Figure 3i, and Table 2 summarizes the orientation index and the order parameter values for all undrawn and drawn nanocomposites films. Both parameters, π and S, range from 0 to 1, with unity corresponding to perfect alignment parallel to the drawing direction and zero corresponding to a random orientation of the crystals. Both methods show a consistent increase for a rising DR, due to the gradual orientation of the films induced by the high humidity drawing procedure. Even the starting films already show a nonzero value, which arises from some preferential in-plane structure formation during the drying. The films with the highest drawing ratio display a very high degree of alignment, around 0.8. This can also be followed after alignment, when placed between crossed polarizers (Figure 4). When placed in parallel with one of the polarizers, the overall image remains dark, while strong birefringence occurs when turned to 45°. This confirms that the aligned films themselves could be used as polarizers.

A direct comparison of the mechanical properties for CNC/CMC nanocomposites as a function of the draw ratio is displayed in Figure 5 and all values are summarized in Table 2. The stress–strain curves of the CNC/CMC films at different DR show a very interesting behavior. Because we found a dependence of the slope of the strain hardening on the DR (see

DOI: 10.1021/am507726t
ACS Appl. Mater. Interfaces 2015, 7, 4595–4607

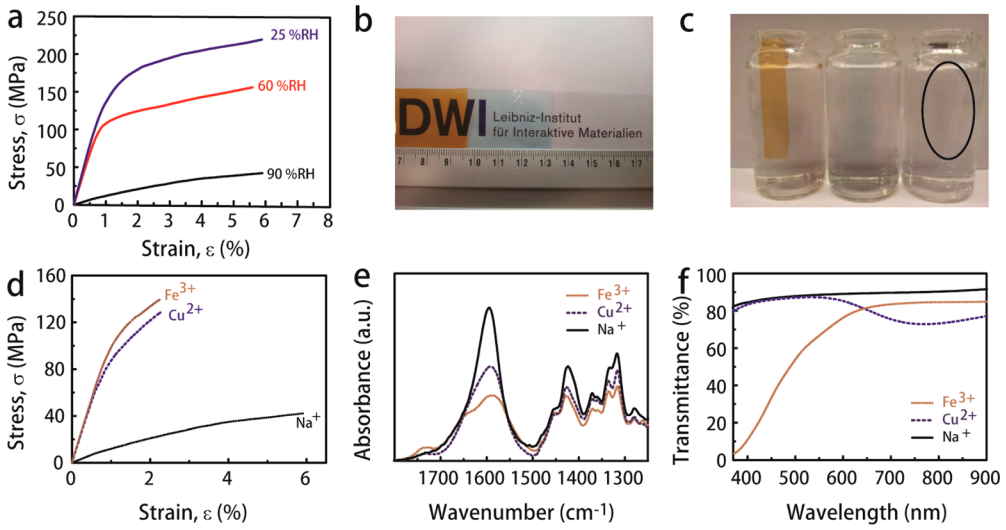

Figure 6. Improved mechanical stability at high relative humidity by modulating supramolecular ionic interactions through counterion exchange within highly aligned CNC/CMC 50/50 w/w nanocomposites at a DR = 2.5. (a) Humidity-dependence of stress/strain curves in tension. Photographs after (b) counterion exchange of (left to right) Fe^{3+}, Cu^{2+}, and Na^{+} and (c) swelling experiments of films displaying stability for the Cu^{2+} and Fe^{3+} infiltrated films while dissolution occurs for the pristine Na^{+} film during the course of hours. (d) Influence of counterion exchange on stress/strain curves in tension at 90% RH. (e) FTIR spectra of the nanocomposites after counterion exchange. (f) VIS spectra of the nanocomposite with various counterions.

below), we conducted the tensile tests at lower strain rate (50% of above) to potentially allow a wider spreading of the slope values. Focusing first on the interpretation of the most obvious differences, one can observe a clear increase in stiffness, yield strength and tensile strength for increasing draw ratios. The tensile strength reaches close to 175 MPa and the Young's modulus reaches 15 GPa, thus showing values that are twice as high as the undrawn film. The increase in stiffness and strength can be understood considering that the CNCs are now more unidirectionally oriented inside the composite and display a more efficient reinforcement. More importantly, however, the drawing procedure does not sacrifice much toughness of the overall materials, as the failure is governed by matrix/interface yielding as favored by the low aspect ratio reinforcements (length/height ≈ 18) and weak interfacial interactions (hydrogen bonds). In contrast to classical nanocomposites, in which higher stiffness and strength are typically obtained at the expense of toughness or strain-at-break, we herein find that higher stiffness and strength can be obtained by increased alignment and without sacrificing much overall work-to-fracture. The films loose some maximum elongation at the early stages of alignment, but then stabilize at similar strain-to-break after reaching drawing ratios of 1.25−1.5. Thereafter the overall tensile curves just show simultaneous increase in all relevant material properties. This behavior leads to a minimum in the work-of-fracture at intermediate drawing ratios and a subsequent increase when progressing to very high degrees of alignment or DRs (Figure 5b). Such a synergetic increase in mechanical properties is highly sought after in bioinspired materials and we show that increasing alignment in highly reinforced nanocomposite materials is a valuable tool to achieve this goal.

For structural materials, it is desirable to have a high Young's modulus and a large elastic region (high yield point), simply because this allows to fully elastically recover larger stresses imparted on a material. Herein, we find that the yield points also consistently increase for higher degree of orientation, which, again, is a beneficial feature for aligned nanocomposites. Furthermore, the alignment leads to distinct changes in the inelastic region, showing a consistent increase of the slope after the yield point with increasing draw ratio (Figure 4c). We suggest that the concurrent orientation of the polymer chains is the main responsible factor.

In summary, the alignment of the highly reinforced CNC/CMC 50/50 w/w nanocomposite toward a bioinspired, nematic type of material allows to synergistically improve the properties in a near bulk, thick film materials. This complements ordering effects pursued for CNC-based 1D fiber materials via spinning techniques, in which the polymer chains are typically drastically more aligned, and goes beyond what ordering techniques for ultrathin CNC films can provide in terms of scalability for mechanical high performance materials.[83−87,97−101]

In the last section, we will address the main drawbacks of waterborne high-performance bioinspired nanocomposites: their susceptibility to water uptake and moisture-induced decrease of mechanical properties. This degradation of properties is mainly due to the competition of water with the hydrogen bonds formed among the building blocks and an occurring plasticization. Sodium carboxymethyl cellulose (Na^{+}CMC) freely dissolves in water depending on the degree of substitution, and thus, its nanocomposites are also affected by the humidity. This can be traced macroscopically by tensile tests at different relative humidities as conducted for the highly aligned nanocomposites with best properties at 50/50 w/w composition and a DR of 2.5. Figure 6a displays the corresponding stress−strain curves and reveals distinct changes at the different relative humidities. The major changes occur when passing from 60 to 90% RH, where a significant loss of stiffness and strength can be observed, while the maximum elongation stays near constant. Both values fall to roughly 5−10% at 90% RH as compared to the dry state (25% RH). The main reasons for a loss in mechanical strength are the loss of hydrogen bonding interactions, due to ingress of water molecules, and the occurring plasticization of the CMC and weakening of the interfacial linkage between CNCs and the

DOI: 10.1021/am507726t
ACS Appl. Mater. Interfaces 2015, 7, 4595−4607

Table 3. Influence of Counterion Exchange on the Mechanical Properties of CNC/CMC (50/50 w/w; DR = 2.5) at 90% Relative Humidity

counterions	Young's modulus, E (GPa)	tensile strength, σ_{UTS} (MPa)	strain at break, ε (%)	work-of-fracture, wof ($MJ \cdot m^{-3}$)
Na^+	1.3 ± 0.4	42 ± 12	6.0 ± 1.5	1.5 ± 0.1
Cu^{2+}	10 ± 2.5	128 ± 26	2.3 ± 0.5	1.9 ± 0.8
Fe^{3+}	11 ± 2.0	140 ± 19	2.3 ± 0.7	2.1 ± 1.0

CMC matrix. The difference between the dry state (25% RH) and the standard testing conditions (60% RH) is only minor, suggesting that hydrogen bonds are still very effective at 60% RH.

Na^+CMC is a weak polyelectrolyte and also the CNCs contain acid groups, and we conceived to change the internal cohesion and matrix/interface interactions by ionic supramolecular bonds using multivalent ions. Previous work on ionic interactions showed that multivalent ions can increase the connectivity in a polymer matrix in nacre-mimetic nanocomposites and induce a stiffening.[54,106] We recently also suggested that it may be a route to stabilize nacre-mimetic nanocomposites at high humidity.[45]

Herein, we target a dedicated strengthening and stability at high relative humidity and focus on strong multivalent ions as complexing agents. In principle, this process allows much better molecular control than, for instance, heating cellulose based nanocomposites or attempting a more random type of chemical cross-linking. To this end, we immersed drawn CNC/CMC (50/50 w/w, DR = 2.5) into 0.1 M $CuSO_4$ and 0.05 M $Fe_2(SO_4)_3$ solution, respectively (details can be found in the Experimental Section). This goes along with a macroscopic hardening of the films inside the salt solutions and bluish (Cu^{2+}) as well as yellowish (Fe^{3+}) films are obtained after extensive washing (Figure 6c). The change in color can be characterized by UV−vis spectroscopy and confirms the successful infiltration with multivalent metal ions (Figure 6b,c,f). Elemental analysis via inductively coupled plasma−atomic emission spectroscopy (ICP-AES) allows to quantify the changes in counterion composition, and we find that the sodium content is reduced from 3.26 wt % (pristine film) to 0.03 and 0.18 wt % for the Fe^{3+}- and Cu^{2+}-infiltrated materials. At the same time, Fe^{3+} and Cu^{2+} can be detected in the respective infiltrated films with 3.60 and 4.80 wt %, while cross-contamination are near or below the detection limit. This corresponds to molar ratios of Na/Cu/Fe of 1:0.53:0.45, which closely reflects the expected changes, albeit with a slight excess of the trivalent Fe^{3+} within the films.

We used Fourier transform infrared (FTIR) spectroscopy to monitor changes in structure upon countering exchange. Figure 6e displays the FTIR spectra in the characteristic range of the carbonyl region. A comparison of Na^+CNC/CMC, Cu^{2+}CNC/CMC and Fe^{3+}CNC/CMC shows little difference in the nature and position of the bands. For Na^+CNC/CMC, a broad band corresponding to asymmetrical stretching mode (υ_{asym}) and a band corresponding to symmetrical stretching mode (υ_{sym}) for COO^- appear at 1594 and 1423 cm^{-1}, respectively. After complexation with Fe^{3+} and Cu^{2+} ions, the asymmetric stretching band broadens slightly while the peak maximum stays near constant (1589 and 1591 cm^{-1}). The symmetrical stretching mode (υ_{asym}) for COO^- shifts to 1427 cm^{-1} and a shoulder is visible at 1450 cm^{-1}. In general, bivalent and trivalent transition metals (Cu^{2+}/Fe^{3+}) have more coordination types than Na^+ such as (1) chelating bidentate or (2) bridging bidentate complexes.[107−110] Interestingly, separate peaks can even be identified in poly(acrylic acid) (PAA)/M^{n+} model compounds, for example, in PAA/Cu(II) at υ_{asym} (COO^-) = 1558 cm^{-1} for chelating bidentate and υ_{asym} (COO^-) = 1611 cm^{-1} for bridging bidentate.[107,108,110] Herein, the υ_{asym} (COO^-) band is so broad that it covers the full region of 1558−1611 cm^{-1}. This indicates that multiple coordination geometries coexist in the material. In principle, for cellulose based polymers, a third type of complexation with the vicinal diols of the sugars might appear for a low degree of substitution and low charge density. Additionally, the CMC chains are also likely to be linked to the CNC surface via complexation to sulfonic acid groups, which leads to further peak broadening. We assured interactions of the multivalent ions with the CNCs by addition of small amounts of Fe^{3+} and Cu^{2+} (2 mmol) to CNC dispersion, whereupon turbidity/light scattering increases due to ion-induced CNC aggregation (Figure S2, Supporting Information). Importantly, we see that very little conversion of Na^+CMC to its acid form takes place during ion exchange. Only a small shoulder is observed at ca. 1733 cm^{-1}, which is shifted compared to pure acidified CMC (1726 cm^{-1}). Overall, these data confirm that indeed the ionic groups are the major structural supramolecular links in the CMC matrix and to the CNC surfaces.

The exchange of the monovalent Na^+ counterion to the bi- and trivalent Cu^{2+} and Fe^{3+} counterions has a pronounced influence on the mechanical properties of the films under hydrated conditions. We focus on the properties at high relative humidity (90% RH) and find a substantial stiffening and strengthening of the films as visible in the tensile testing curves depicted in Figure 6d and summarized in Table 3. We find little traceable differences between the valencies of the counterions, although one could have expected a more pronounced influence as they serve as ionic cross-links with different valency and electrostatic potential. This behavior may stem from after all rather similar complex geometries within the bulk phase. The stiffness of the films increase one order of magnitude from ca. 1.3 GPa in Na^+CNC/CMC to 10 and 11 GPa for Cu^{2+}CNC/CMC or Fe^{3+}CNC/CMC, respectively. At the same time, the tensile strength triples to just above 125 MPa. Although a loss of strain-at-break is observed, the substantially increased stiffness and strength can balance the overall properties and lead to ca. 25% increase in the wof. Considering the highly hydrated state of these materials at 90% RH, we find an attractive mechanical performance for such waterborne high performance materials.

CONCLUSION

We demonstrated a simple and straightforward experimental approach to achieve unidirectional mesoscale alignment of cellulose nanocrystals within polymer matrixes by drawing under plasticized conditions. To the best of our knowledge, these are some of the first thick and highly aligned all-cellulose-type nanocomposites using cellulose nanocrystals. The nematic type unidirectional ordering is reminiscent of the structures found in biological materials and can even be achieved at a high

DOI: 10.1021/am507726t
ACS Appl. Mater. Interfaces 2015, 7, 4595−4607

level of reinforcements (here, 50 wt %). Our structural model also explains that a minimum of polymer content has to be present to prevent direct contacts between reinforcements in a space filling hexagonal packing of infinite cylinders of a given diameter.

The importance of the alignment manifests in displaying synergetic increases of stiffness, strength, and toughness at the same composition, simply by increasing the level of alignment of the nanoscale reinforcements. In a more applied context, it means that possibilities for alignment of CNCs within matrixes have to be found that are compatible with larger scale processing (e.g., calendaring of thick films).

We could further show that the decline in mechanical properties of such waterborne all-biobased nanocomposites can be prevented using supramolecular modulation of the ionic interactions inside the CMC matrix, as well as between CNC and CMC, by exchanging the monovalent Na^+ with di- or trivalent Cu^{2+} and Fe^{3+}. Similarly, this leads to a synergetic improvement of the mechanical properties, and an attractive overall performance with greater than 10 GPa in stiffness and 125 MPa in tensile strength can be realized at 90% relative humidity. Although the ion valency does not manifest in significant differences at this point, we suggest that using different ion combinations and different types of cations (such as substituted ammonium ions) will enable further manipulation of the interactions and targeting sacrificial bonds with stick/slip interactions.

■ ASSOCIATED CONTENT

Supporting Information

AFM and ion-induced aggregation of CNCs. This material is available free of charge via the Internet at http://pubs.acs.org.

■ AUTHOR INFORMATION

Corresponding Author

*E-mail: walther@dwi.rwth-aachen.de.

Notes

The authors declare no competing financial interest.

■ ACKNOWLEDGMENTS

We acknowledge financial support from the BMBF in the framework of the AQUAMAT research group and the CSC for a scholarship. We are grateful for access at the Shanghai synchrotron radiation facilities. A.W. gratefully acknowledges continuous support by Martin Möller.

■ REFERENCES

(1) Gindl, W. Cellulose Fibril- and Whisker-Reinforced Polymer Nanocomposites. In *Recent Advances in Polymer Nanocomposites*. Thomas, S., Zaikov, G. E., Valsaraj, S. V., Eds.; VSP: Boston, 2009; pp 269−284.

(2) Tingaut, P.; Zimmermann, T.; Sebe, G. Cellulose Nanocrystals and Microfibrillated Cellulose as Building Blocks for the Design of Hierarchical Functional Materials. *J. Mater. Chem.* **2012**, *22*, 20105−20111.

(3) Xu, X.; Liu, F.; Jiang, L.; Zhu, J. Y.; Haagenson, D.; Wiesenborn, D. P. Cellulose Nanocrystals vs. Cellulose Nanofibrils: A Comparative Study on Their Microstructures and Effects as Polymer Reinforcing Agents. *ACS Appl. Mater. Interfaces* **2013**, *5*, 2999−3009.

(4) Habibi, Y.; Lucia, L. A.; Rojas, O. J. Cellulose Nanocrystals: Chemistry, Self-Assembly, and Applications. *Chem. Rev.* **2010**, *110*, 3479−500.

(5) Moon, R. J.; Martini, A.; Nairn, J.; Simonsen, J.; Youngblood, J. Cellulose Nanomaterials Review: Structure, Properties, and Nanocomposites. *Chem. Soc. Rev.* **2011**, *40*, 3941−3994.

(6) Kalia, S.; Dufresne, A.; Cherian, B. M.; Kaith, B. S.; Avérous, L.; Njuguna, J.; Nassiopoulos, E. Cellulose-Based Bio- and Nanocomposites: A Review. *Int. J. Polym. Sci.* **2011**, *2011*, 1−35.

(7) Peng, B. L.; Dhar, N.; Liu, H. L.; Tam, K. C. Chemistry and Applications of Nanocrystalline Cellulose and Its Derivatives: A Nanotechnology Perspective. *Can. J. Chem. Eng.* **2011**, *89*, 1191−1206.

(8) Siró, I.; Plackett, D. Microfibrillated Cellulose and New Nanocomposite Materials: A Review. *Cellulose* **2010**, *17*, 459−494.

(9) Spence, K.; Habibi, Y.; Dufresne, A. *Nanocellulose-Based Composites*. Springer: Berlin Heidelberg, 2011; pp 179−213.

(10) Klemm, D.; Schumann, D.; Kramer, F.; Heßler, N.; Hornung, M.; Schmauder, H.-P.; Marsch, S. *Nanocelluloses as Innovative Polymers in Research and Application*. Springer: Berlin Heidelberg, 2006; pp 49−96.

(11) Klemm, D.; Kramer, F.; Moritz, S.; Lindstrom, T.; Ankerfors, M.; Gray, D.; Dorris, A. Nanocelluloses: A New Family of Nature-Based Materials. *Angew. Chem., Int. Ed.* **2011**, *50*, 5438−5466.

(12) Lin, N.; Huang, J.; Dufresne, A. Preparation, Properties, and Applications of Polysaccharide Nanocrystals in Advanced Functional Nanomaterials: A Review. *Nanoscale* **2012**, *4*, 3274−3294.

(13) Zhou, C.; Wu, Q. Recent Development in Applications of Cellulose Nanocrystals for Advanced Polymer-Based Nanocomposites by Novel Fabrication Strategies. *Nanocrystals—Synthesis, Characterization, and Applications*. Nerella, S., Ed.; InTech: Rijeka, Croatia, **2012**; pp 102−120.

(14) Dong, X.; Revol, J.-F.; Gray, D. Effect of Microcrystallite Preparation Conditions on the Formation of Colloid Crystals of Cellulose. *Cellulose* **1998**, *5*, 19−32.

(15) Araki, J.; Wada, M.; Kuga, S.; Okano, T. Birefringent Glassy Phase of a Cellulose Microcrystal Suspension. *Langmuir* **2000**, *16*, 2413−2415.

(16) Habibi, Y.; Goffin, A.-L.; Schiltz, N.; Duquesne, E.; Dubois, P.; Dufresne, A. Bionanocomposites Based on Poly(ε-Caprolactone)-Grafted Cellulose Nanocrystals by Ring-Opening Polymerization. *J. Mater. Chem.* **2008**, *18*, 5002−5010.

(17) Garcia de Rodriguez, N. L.; Thielemans, W.; Dufresne, A. Sisal Cellulose Whiskers Reinforced Polyvinyl Acetate Nanocomposites. *Cellulose* **2006**, *13*, 261−270.

(18) Habibi, Y.; Dufresne, A. Highly Filled Bionanocomposites from Functionalized Polysaccharide Nanocrystals. *Biomacromolecules* **2008**, *9*, 1974−1980.

(19) Habibi, Y.; Foulon, L.; Aguié-Béghin, V.; Molinari, M.; Douillard, R. Langmuir−Blodgett Films of Cellulose Nanocrystals: Preparation and Characterization. *J. Colloid Interface Sci.* **2007**, *316*, 388−397.

(20) Cao, X.; Chen, Y.; Chang, P. R.; Stumborg, M.; Huneault, M. A. Green Composites Reinforced with Hemp Nanocrystals in Plasticized Starch. *J. Appl. Polym. Sci.* **2008**, *109*, 3804−3810.

(21) Cao, X.; Dong, H.; Li, C. M. New Nanocomposite Materials Reinforced with Flax Cellulose Nanocrystals in Waterborne Polyurethane. *Biomacromolecules* **2007**, *8*, 899−904.

(22) Siqueira, G.; Bras, J.; Dufresne, A. Cellulose Whiskers versus Microfibrils: Influence of the Nature of the Nanoparticle and its Surface Functionalization on the Thermal and Mechanical Properties of Nanocomposites. *Biomacromolecules* **2009**, *10*, 425−432.

(23) Helbert, W.; Cavaillé, J. Y.; Dufresne, A. Thermoplastic Nanocomposites Filled with Wheat Straw Cellulose Whiskers. Part I: Processing and Mechanical Behavior. *Polym. Compos.* **1996**, *17*, 604−611.

(24) Bendahou, A.; Habibi, Y.; Kaddami, H.; Dufresne, A. Physico-Chemical Characterization of Palm from Phoenix Dactylifera−L, Preparation of Cellulose Whiskers and Natural Rubber−Based Nanocomposites. *J. Biobased Mater. Bioenergy* **2009**, *3*, 81−90.

(25) Araki, J.; Wada, M.; Kuga, S.; Okano, T. Influence of Surface Charge on Viscosity Behavior of Cellulose Microcrystal Suspension. *J. Wood Sci.* **1999**, *45*, 258−261.

DOI: 10.1021/am507726t
ACS Appl. Mater. Interfaces 2015, 7, 4595−4607

(26) Beck-Candanedo, S.; Roman, M.; Gray, D. G. Effect of Reaction Conditions on the Properties and Behavior of Wood Cellulose Nanocrystal Suspensions. *Biomacromolecules* **2005**, *6*, 1048−1054.
(27) Cao, X.; Habibi, Y.; Lucia, L. A. One-Pot Polymerization, Surface Grafting, and Processing of Waterborne Polyurethane-Cellulose Nanocrystal Nanocomposites. *J. Mater. Chem.* **2009**, *19*, 7137−7145.
(28) Bondeson, D.; Mathew, A.; Oksman, K. Optimization of the Isolation of Nanocrystals from Microcrystalline Cellulose by Acid Hydrolysis. *Cellulose* **2006**, *13*, 171−180.
(29) Pranger, L.; Tannenbaum, R. Biobased Nanocomposites Prepared by In Situ Polymerization of Furfuryl Alcohol with Cellulose Whiskers or Montmorillonite Clay. *Macromolecules* **2008**, *41*, 8682−8687.
(30) Capadona, J. R.; Shanmuganathan, K.; Trittschuh, S.; Seidel, S.; Rowan, S. J.; Weder, C. Polymer Nanocomposites with Nanowhiskers Isolated from Microcrystalline Cellulose. *Biomacromolecules* **2009**, *10*, 712−716.
(31) Grunert, M.; Winter, W. Nanocomposites of Cellulose Acetate Butyrate Reinforced with Cellulose Nanocrystals. *J. Polym. Environ.* **2002**, *10*, 27−30.
(32) Araki, J.; Kuga, S. Effect of Trace Electrolyte on Liquid Crystal Type of Cellulose Microcrystals. *Langmuir* **2001**, *17*, 4493−4496.
(33) Hirai, A.; Inui, O.; Horii, F.; Tsuji, M. Phase Separation Behavior in Aqueous Suspensions of Bacterial Cellulose Nanocrystals Prepared by Sulfuric Acid Treatment. *Langmuir* **2009**, *25*, 497−502.
(34) Anglès, M. N.; Dufresne, A. Plasticized Starch/Tunicin Whiskers Nanocomposite Materials. 2. Mechanical Behavior. *Macromolecules* **2001**, *34*, 2921−2931.
(35) de Souza Lima, M. M.; Borsali, R. Static and Dynamic Light Scattering from Polyelectrolyte Microcrystal Cellulose. *Langmuir* **2002**, *18*, 992−996.
(36) Anglès, M. N.; Dufresne, A. Plasticized Starch/Tunicin Whiskers Nanocomposites. 1. Structural Analysis. *Macromolecules* **2000**, *33*, 8344−8353.
(37) Samir, M. A. S. A.; Alloin, F.; Dufresne, A. Review of Recent Research into Cellulosic Whiskers, Their Properties and Their Application in Nanocomposite Field. *Biomacromolecules* **2005**, *6*, 612−626.
(38) Sturcova, A.; Davies, G. R.; Eichhorn, S. J. Elastic Modulus and Stress-Transfer Properties of Tunicate Cellulose Whiskers. *Biomacromolecules* **2005**, *6*, 1055−1061.
(39) Sinko, R.; Mishra, S.; Ruiz, L.; Brandis, N.; Keten, S. Dimensions of Biological Cellulose Nanocrystals Maximize Fracture Strength. *ACS Macro Lett.* **2013**, *3*, 64−69.
(40) Meyers, M. A.; Chen, P.-Y.; Lin, A. Y.-M.; Seki, Y. Biological Materials: Structure and Mechanical Properties. *Prog. Mater. Sci.* **2008**, *53*, 1−206.
(41) Burgert, I.; Fratzl, P. Actuation Systems in Plants as Prototypes for Bioinspired Devices. *Philos. Trans. R. Soc., A* **2009**, *367*, 1541−1557.
(42) Chen, P.-Y.; McKittrick, J.; Meyers, M. A. Biological Materials: Functional Adaptations and Bioinspired Designs. *Prog. Mater. Sci.* **2012**, *57*, 1492−1704.
(43) Sinha Ray, S.; Okamoto, M. Polymer/Layered Silicate Nanocomposites: A Review from Preparation to Processing. *Prog. Mater. Sci.* **2003**, *28*, 1539−1641.
(44) Das, P.; Schipmann, S.; Malho, J.-M.; Zhu, B.; Klemradt, U.; Walther, A. Facile Access to Large-Scale, Self-Assembled, Nacre-Inspired, High-Performance Materials with Tunable Nanoscale Periodicities. *ACS Appl. Mater. Interfaces* **2013**, *5*, 3738−3747.
(45) Das, P.; Walther, A. Ionic Supramolecular Bonds Preserve Mechanical Properties and Enable Synergetic Performance at High Humidity in Water-Borne, Self-Assembled Nacre-Mimetics. *Nanoscale* **2013**, *5*, 9348−9356.
(46) Wang, J.; Cheng, Q.; Lin, L.; Jiang, L. Synergistic Toughening of Bioinspired Poly(Vinyl Alcohol)−Clay−Nanofibrillar Cellulose Artificial Nacre. *ACS Nano* **2014**, *8*, 2739−2745.
(47) Kaushik, A. K.; Podsiadlo, P.; Qin, M.; Shaw, C. M.; Waas, A. M.; Kotov, N. A.; Arruda, E. M. The Role of Nanoparticle Layer Separation in the Finite Deformation Response of Layered Polyurethane-Clay Nanocomposites. *Macromolecules* **2009**, *42*, 6588−6595.
(48) Podsiadlo, P.; Kaushik, A. K.; Arruda, E. M.; Waas, A. M.; Shim, B. S.; Xu, J.; Nandivada, H.; Pumplin, B. G.; Lahann, J.; Ramamoorthy, A.; Kotov, N. A. Ultrastrong and Stiff Layered Polymer Nanocomposites. *Science* **2007**, *318*, 80−83.
(49) Verho, T.; Karesoja, M.; Das, P.; Martikainen, L.; Lund, R.; Alegría, A.; Walther, A.; Ikkala, O. Hydration and Dynamic State of Nanoconfined Polymer Layers Govern Toughness in Nacre-Mimetic Nanocomposites. *Adv. Mater.* **2013**, *25*, 5055−5059.
(50) Martikainen, L.; Walther, A.; Seitsonen, J.; Berglund, L.; Ikkala, O. Deoxyguanosine Phosphate Mediated Sacrificial Bonds Promote Synergistic Mechanical Properties in Nacre-Mimetic Nanocomposites. *Biomacromolecules* **2013**, *14*, 2531−2535.
(51) Kochumalayil, J. J.; Morimune, S.; Nishino, T.; Ikkala, O.; Walther, A.; Berglund, L. A. Nacre-Mimetic Clay/Xyloglucan Bionanocomposites: A Chemical Modification Route for Hygromechanical Performance at High Humidity. *Biomacromolecules* **2013**, *14*, 3842−3849.
(52) Tang, Z.; Kotov, N. A.; Magonov, S.; Ozturk, B. Nanostructured Artificial Nacre. *Nat. Mater.* **2003**, *2*, 413−418.
(53) Walther, A.; Bjurhager, I.; Malho, J.-M.; Pere, J.; Ruokolainen, J.; Berglund, L. A.; Ikkala, O. Large-Area, Lightweight, and Thick Biomimetic Composites with Superior Material Properties via Fast, Economic, and Green Pathways. *Nano Lett.* **2010**, *10*, 2742−2748.
(54) Walther, A.; Bjurhager, I.; Malho, J.-M.; Ruokolainen, J.; Berglund, L.; Ikkala, O. Supramolecular Control of Stiffness and Strength in Lightweight High-Performance Nacre-Mimetic Paper with Fire-Shielding Properties. *Angew. Chem., Int. Ed.* **2010**, *49*, 6448−6453.
(55) Isogai, A.; Saito, T.; Fukuzumi, H. TEMPO-Oxidized Cellulose Nanofibers. *Nanoscale* **2011**, *3*, 71−85.
(56) Saito, T.; Uematsu, T.; Kimura, S.; Enomae, T.; Isogai, A. Self-Aligned Integration of Native Cellulose Nanofibrils Towards Producing Diverse Bulk Materials. *Soft Matter* **2011**, *7*, 8804−8809.
(57) Sehaqui, H.; Zhou, Q.; Ikkala, O.; Berglund, L. A. Strong and Tough Cellulose Nanopaper with High Specific Surface Area and Porosity. *Biomacromolecules* **2011**, *12*, 3638−3644.
(58) Henriksson, M.; Berglund, L. A.; Isaksson, P.; Lindström, T.; Nishino, T. Cellulose Nanopaper Structures of High Toughness. *Biomacromolecules* **2008**, *9*, 1579−1585.
(59) Sehaqui, H.; Ezekiel Mushi, N.; Morimune, S.; Salajkova, M.; Nishino, T.; Berglund, L. A. Cellulose Nanofiber Orientation in Nanopaper and Nanocomposites by Cold Drawing. *ACS Appl. Mater. Interfaces* **2012**, *4*, 1043−1049.
(60) Wu, C.-N.; Yang, Q.; Takeuchi, M.; Saito, T.; Isogai, A. Highly Tough and Transparent Layered Composites of Nanocellulose and Synthetic Silicate. *Nanoscale* **2014**, *6*, 392−399.
(61) Saito, T.; Oaki, Y.; Nishimura, T.; Isogai, A.; Kato, T. Bioinspired Stiff and Flexible Composites of Nanocellulose-Reinforced Amorphous $CaCO_3$. *Mater. Horiz.* **2014**, *1*, 321−325.
(62) Sehaqui, H.; Zhou, Q.; Berglund, L. A. Nanostructured Biocomposites of High Toughness—A Wood Cellulose Nanofiber Network in Ductile Hydroxyethylcellulose Matrix. *Soft Matter* **2011**, *7*, 7342−7350.
(63) Sehaqui, H.; Liu, A.; Zhou, Q.; Berglund, L. A. Fast Preparation Procedure for Large, Flat Cellulose and Cellulose/Inorganic Nanopaper Structures. *Biomacromolecules* **2010**, *11*, 2195−2198.
(64) Sehaqui, H.; Morimune, S.; Nishino, T.; Berglund, L. A. Stretchable and Strong Cellulose Nanopaper Structures Based on Polymer-Coated Nanofiber Networks: An Alternative to Nonwoven Porous Membranes from Electrospinning. *Biomacromolecules* **2012**, *13*, 3661−3667.
(65) Utsel, S.; Malmstrom, E. E.; Carlmark, A.; Wagberg, L. Thermoresponsive Nanocomposites from Multilayers of Nanofibrillated Cellulose and Specially Designed N-Isopropylacrylamide Based Polymers. *Soft Matter* **2010**, *6*, 342−352.

DOI: 10.1021/am507726t
ACS Appl. Mater. Interfaces 2015, 7, 4595−4607

(66) Acciaro, R.; Aulin, C.; Wagberg, L.; Lindstrom, T.; Claesson, P. M.; Varga, I. Investigation of the Formation, Structure and Release Characteristics of Self-Assembled Composite Films of Cellulose Nanofibrils and Temperature Responsive Microgels. *Soft Matter* **2011**, *7*, 1369−1377.
(67) Karabulut, E.; Wagberg, L. Design and Characterization of Cellulose Nanofibril-Based Freestanding Films Prepared by Layer-By-Layer Deposition Technique. *Soft Matter* **2011**, *7*, 3467−3474.
(68) Fall, A. B.; Lindstrom, S. B.; Sprakel, J.; Wagberg, L. A Physical Cross-Linking Process of Cellulose Nanofibril Gels with Shear-Controlled Fibril Orientation. *Soft Matter* **2013**, *9*, 1852−1863.
(69) Liu, A.; Walther, A.; Ikkala, O.; Belova, L.; Berglund, L. A. Clay Nanopaper with Tough Cellulose Nanofiber Matrix for Fire Retardancy and Gas Barrier Functions. *Biomacromolecules* **2011**, *12*, 633−641.
(70) Walther, A.; Timonen, J. V. I; Díez, I.; Laukkanen, A.; Ikkala, O. Multifunctional High-Performance Biofibers Based on Wet-Extrusion of Renewable Native Cellulose Nanofibrils. *Adv. Mater.* **2011**, *23*, 2924−2928.
(71) Torres-Rendon, J. G.; Schacher, F. H.; Ifuku, S.; Walther, A. Mechanical Performance of Macrofibers of Cellulose and Chitin Nanofibrils Aligned by Wet-Stretching: A Critical Comparison. *Biomacromolecules* **2014**, *15*, 2709−2717.
(72) Iwamoto, S.; Isogai, A.; Iwata, T. Structure and Mechanical Properties of Wet-Spun Fibers Made from Natural Cellulose Nanofibers. *Biomacromolecules* **2011**, *12*, 831−836.
(73) Svagan, A. J.; Berglund, L. A.; Jensen, P. Cellulose Nanocomposite Biopolymer Foam—Hierarchical Structure Effects on Energy Absorption. *ACS Appl. Mater. Interfaces* **2011**, *3*, 1411−1417.
(74) Svagan, A. J.; Samir, M. A. S. A.; Berglund, L. A. Biomimetic Foams of High Mechanical Performance Based on Nanostructured Cell Walls Reinforced by Native Cellulose Nanofibrils. *Adv. Mater.* **2008**, *20*, 1263−1269.
(75) Aulin, C.; Netrval, J.; Wagberg, L.; Lindstrom, T. Aerogels from Nanofibrillated Cellulose with Tunable Oleophobicity. *Soft Matter* **2010**, *6*, 3298−3305.
(76) Sugiyama, J.; Chanzy, H.; Maret, G. Orientation of Cellulose Microcrystals by Strong Magnetic Fields. *Macromolecules* **1992**, *25*, 4232−4234.
(77) Revol, J.-F.; Godbout, L.; Dong, X.-M.; Gray, D. G.; Chanzy, H.; Maret, G. Chiral Nematic Suspensions of Cellulose Crystallites; Phase Separation and Magnetic Field Orientation. *Liq. Cryst.* **1994**, *16*, 127−134.
(78) Kimura, F.; Kimura, T.; Tamura, M.; Hirai, A.; Ikuno, M.; Horii, F. Magnetic Alignment of the Chiral Nematic Phase of a Cellulose Microfibril Suspension. *Langmuir* **2005**, *21*, 2034−2037.
(79) Kvien, I.; Oksman, K. Orientation of Cellulose Nanowhiskers in Polyvinyl Alcohol. *Appl. Phys. A: Mater. Sci. Process.* **2007**, *87*, 641−643.
(80) Bordel, D.; Putaux, J.-L.; Heux, L. Orientation of Native Cellulose in an Electric Field. *Langmuir* **2006**, *22*, 4899−4901.
(81) Habibi, Y.; Heim, T.; Douillard, R. AC Electric Field-Assisted Assembly and Alignment of Cellulose Nanocrystals. *J. Polym. Sci., Part B: Polym. Phys.* **2008**, *46*, 1430−1436.
(82) Gindl, W.; Emsenhuber, G.; Maier, G.; Keckes, J. Cellulose in Never-Dried Gel Oriented by an AC Electric Field. *Biomacromolecules* **2009**, *10*, 1315−1318.
(83) Hoeger, I.; Rojas, O. J.; Efimenko, K.; Velev, O. D.; Kelley, S. S. Ultrathin Film Coatings of Aligned Cellulose Nanocrystals from a Convective-Shear Assembly System and Their Surface Mechanical Properties. *Soft Matter* **2011**, *7*, 1957−1967.
(84) Diaz, J. A.; Wu, X.; Martini, A.; Youngblood, J. P.; Moon, R. J. Thermal Expansion of Self-Organized and Shear-Oriented Cellulose Nanocrystal Films. *Biomacromolecules* **2013**, *14*, 2900−2908.
(85) Reising, A. B.; Moon, R. J.; Youngblood, J. P. Effect of Particle Alignment on Mechanical Properties of Neat Cellulose Nanocrystal Films. *J. Sci. Technol. For. Prod. Processes* **2013**, *2*, 32−41.
(86) Yoshiharu, N.; Shigenori, K.; Masahisa, W.; Takeshi, O. Cellulose Microcrystal Film of High Uniaxial Orientation. *Macromolecules* **1997**, *30*, 6395−6397.
(87) Csoka, L.; Hoeger, I. C.; Peralta, P.; Peszlen, I.; Rojas, O. J. Dielectrophoresis of Cellulose Nanocrystals and Alignment in Ultrathin Films by Electric Field-Assisted Shear Assembly. *J. Colloid Interface Sci.* **2011**, *363*, 206−212.
(88) Nishiyama, Y.; Kuga, S.; Wada, M.; Okano, T. Cellulose Microcrystal Film of High Uniaxial Orientation. *Macromolecules* **1997**, *30*, 6395−6397.
(89) Shopsowitz, K. E.; Qi, H.; Hamad, W. Y.; MacLachlan, M. J. Free-Standing Mesoporous Silica Films with Tunable Chiral Nematic Structures. *Nature* **2010**, *468*, 422−425.
(90) Shopsowitz, K. E.; Hamad, W. Y.; MacLachlan, M. J. Flexible and Iridescent Chiral Nematic Mesoporous Organosilica Films. *J. Am. Chem. Soc.* **2011**, *134*, 867−870.
(91) Giese, M.; Khan, M. K.; Hamad, W. Y.; MacLachlan, M. J. Imprinting of Photonic Patterns with Thermosetting Amino-Formaldehyde-Cellulose Composites. *ACS Macro Lett.* **2013**, *2*, 818−821.
(92) Kelly, J. A.; Shukaliak, A. M.; Cheung, C. C. Y.; Shopsowitz, K. E.; Hamad, W. Y.; MacLachlan, M. J. Responsive Photonic Hydrogels Based on Nanocrystalline Cellulose. *Angew. Chem., Int. Ed.* **2013**, *52*, 8912−8916.
(93) Khan, M. K.; Giese, M.; Yu, M.; Kelly, J. A.; Hamad, W. Y.; MacLachlan, M. J. Flexible Mesoporous Photonic Resins with Tunable Chiral Nematic Structures. *Angew. Chem., Int. Ed.* **2013**, *52*, 8921−8924.
(94) Shopsowitz, K. E.; Kelly, J. A.; Hamad, W. Y.; MacLachlan, M. J. Biopolymer Templated Glass with a Twist: Controlling the Chirality, Porosity, and Photonic Properties of Silica with Cellulose Nanocrystals. *Adv. Funct. Mater.* **2013**, *24*, 327−338.
(95) Giese, M.; Blusch, L. K.; Khan, M. K.; Hamad, W. Y.; MacLachlan, M. J. Responsive Mesoporous Photonic Cellulose Films by Supramolecular Cotemplating. *Angew. Chem., Int. Ed.* **2014**, *53*, 8880−8884.
(96) Cheung, C. C. Y.; Giese, M.; Kelly, J. A.; Hamad, W. Y.; MacLachlan, M. J. Iridescent Chiral Nematic Cellulose Nanocrystal/Polymer Composites Assembled in Organic Solvents. *ACS Macro Lett.* **2013**, *2*, 1016−1020.
(97) Chen, S.; Schueneman, G.; Pipes, R. B.; Youngblood, J. P.; Moon, R. J. Effects of Crystal Orientation on Cellulose Nanocrystals-Cellulose Acetate Nanocomposite Fibers Prepared by Dry Spinning. *Biomacromolecules* **2014**, *15*, 3827−3835.
(98) Ureña-Benavides, E. E.; Kitchens, C. L. Wide-Angle X-Ray Diffraction of Cellulose Nanocrystal−Alginate Nanocomposite Fibers. *Macromolecules* **2011**, *44*, 3478−3484.
(99) Ureña-Benavides, E. E.; Brown, P. J.; Kitchens, C. L. Effect of Jet Stretch and Particle Load on Cellulose Nanocrystal−Alginate Nanocomposite Fibers. *Langmuir* **2010**, *26*, 14263−14270.
(100) Peresin, M. S.; Vesterinen, A.-H.; Habibi, Y.; Johansson, L.-S.; Pawlak, J. J.; Nevzorov, A. A.; Rojas, O. J. Crosslinked PVA Nanofibers Reinforced with Cellulose Nanocrystals: Water Interactions and Thermomechanical Properties. *J. Appl. Polym. Sci.* **2014**, *131*, 327−338.
(101) Jalal Uddin, A.; Araki, J.; Gotoh, Y. Toward "Strong" Green Nanocomposites: Polyvinyl Alcohol Reinforced with Extremely Oriented Cellulose Whiskers. *Biomacromolecules* **2011**, *12*, 617−624.
(102) Benítez, A. J.; Torres-Rendon, J.; Poutanen, M.; Walther, A. Humidity and Multiscale Structure Govern Mechanical Properties and Deformation Modes in Films of Native Cellulose Nanofibrils. *Biomacromolecules* **2013**, *14*, 4497−4506.
(103) Choi, Y. J.; Simonsen, J. Cellulose Nanocrystal-filled Carboxymethyl Cellulose Nanocomposites. *J. Nanosci. Nanotechnol.* **2006**, *6*, 633−639.
(104) Ranby, B. G.; Ribi, E. Die Feinstruktur der Zellulose. *Experimentia* **1950**, *6*, 12−14.
(105) Marchessault, R. H.; Morehead, F. F.; Walter, N. M. Liquid Crystal Systems from Fibrillar Polysaccharides. *Nature* **1959**, *184*, 632−633.

DOI: 10.1021/am507726t
ACS Appl. Mater. Interfaces 2015, 7, 4595−4607

(106) Podsiadlo, P.; Kaushik, A. K.; Shim, B. S.; Agarwal, A.; Tang, Z.; Waas, A. M.; Arruda, E. M.; Kotov, N. A. Can Nature's Design be Improved Upon? High Strength, Transparent Nacre-Like Nanocomposites with Double Network of Sacrificial Cross Links. *J. Phys. Chem. B* **2008**, *112*, 14359−14363.
(107) Konradi, R.; Rühe, J. Interaction of Poly(Methacrylic Acid) Brushes with Metal Ions: Swelling Properties. *Macromolecules* **2005**, *38*, 4345−4354.
(108) Konradi, R.; Rühe, J. Interaction of Poly(Methacrylic Acid) Brushes with Metal Ions: An Infrared Investigation. *Macromolecules* **2004**, *37*, 6954−6961.
(109) He, F.; Zhao, D.; Liu, J.; Roberts, C. B. Stabilization of Fe−Pd Nanoparticles with Sodium Carboxymethyl Cellulose for Enhanced Transport and Dechlorination of Trichloroethylene in Soil and Groundwater. *Ind. Eng. Chem. Res.* **2006**, *46*, 29−34.
(110) McCluskey, P. H.; Snyder, R. L.; Condrate, R. A., Sr. Infrared Spectral Studies of Various Metal Polyacrylates. *J. Solid State Chem.* **1989**, *83*, 332−339.

DOI: 10.1021/am507726t
ACS Appl. Mater. Interfaces 2015, 7, 4595−4607